frontiers | Frontiers in Materials

TYPE Original Research
PUBLISHED 09 November 2023
DOI 10.3389/fmats.2023.1298188

OPEN ACCESS

EDITED BY
Gabseok Seo,
Frontier Energy Solution, Republic of Korea

REVIEWED BY
Seunghwan Bae,
Korea Institute of Industrial Technology, Republic of Korea
Jae-Yup Kim,
Dankook University, Republic of Korea
Ahmed Mourtada Elseman,
Central Metallurgical Research and Development Institute (CMRDI), Egypt

*CORRESPONDENCE
Bonkee Koo,
bonkeekoo@hanyang.ac.kr
Min Jae Ko,
mjko@hanyang.ac.kr
Heesuk Jung,
spes@kist.re.kr

RECEIVED 21 September 2023
ACCEPTED 26 October 2023
PUBLISHED 09 November 2023

CITATION
Kim W, Koo B, Ko MJ and Jung H (2023), Hot-injection synthesis of lead-free pseudo-alkali metal-based perovskite ($TlSnX_3$) nanoparticles with tunable optical properties.
Front. Mater. 10:1298188.
doi: 10.3389/fmats.2023.1298188

Hot-injection synthesis of lead-free pseudo-alkali metal-based perovskite ($TlSnX_3$) nanoparticles with tunable optical properties

Wooyeon Kim[1], Bonkee Koo[1]*, Min Jae Ko[1]* and Heesuk Jung[2]*

[1]Department of Chemical Engineering, Hanyang University, Seoul, Republic of Korea, [2]Advanced Photovoltaics Research Center, Korea Institute of Science and Technology (KIST), Seoul, Republic of Korea

The commercialization of organo-inorganic hybrid perovskite materials for optoelectronic applications is limited owing to the restriction of lead (Pb) usage in consumer electronics and the instability of organic cations in the perovskite structure. To address these challenges, we synthesize $TlSnX_3$ (X = Cl, Br, and I) perovskite nanoparticles (NPs) with high crystallinity and uniformity using the hot-injection method. The optical properties of $TlSnX_3$ NPs are fine-tuned by substituting the halide ions of $TlSnX_3$. In addition, the oxidation of Sn in $TlSnX_3$ NPs is effectively prevented by the strong reducing ligands such as dioleamide (DOA) and trioctylphosphine (TOP). Furthermore, $TlSnX_3$ NPs-based perovskite solar cells (PSCs) are fabricated by a spin-coating method; they exhibited a high open-circuit voltage (~1.4 V). These results demonstrate that $TlSnX_3$ NPs can be an attractive candidate for solution-processable optoelectronic devices.

KEYWORDS

lead-free pseudo-alkali metal halide perovskite, nanocrystals, dioleamide ligands, perovskite solar cells, optoelectronics

Introduction

Organo-inorganic hybrid perovskite materials are emerging as the most promising candidates for optoelectronic applications such as photovoltaics, light-emitting diodes, photodetectors, and lasers (Xing et al., 2013; Xing et al., 2014; Cho et al., 2015; Zhu et al., 2015; Kwon et al., 2023; Zhang et al., 2023). Organo-inorganic hybrid perovskites are chemical compounds with the structural formula ABX_3, where the A site is occupied by an organic ammonium ion ($CH_3NH_3^+$ and $HC(NH_2)_2^+$), B is a p-block metal cation (Sn^{2+} and Pb^{2+}), and X is a halide anion (Cl^-, Br^-, and I^-). Recently, organo-inorganic hybrid perovskites based on lead (Pb) ion at the B site have attracted significant attention because perovskite solar cells (PSCs) based on them have shown a certified photoconversion efficiency (PCE) of 26.1% (National Renewable Energy Laboratory, 2023). Furthermore, light-emitting diodes based on $CH_3NH_3PbX_3$ (X = halide ion) exhibit a high external quantum efficiency because they have high color purity (Cho et al., 2015). Their unique optoelectronic properties demonstrated that perovskites based on Pb are one of the strongest candidates for next-generation optoelectronic devices (Xing et al., 2013; Xing et al., 2014; Cho et al., 2015; Zhu et al., 2015).

However, the main challenge in the commercialization of Pb-based perovskite materials is the European Union restriction on Pb-containing materials in consumer electronics (Restriction of Hazardous Substances, RoHS) (Luo et al., 2022; Pancini et al., 2023). Thus, tin (Sn) has been suggested as an alternative p-block metal cation for Pb-free perovskite materials (Takahashi et al., 2011; Cao and Yan, 2021). The electrical properties of an Sn-based perovskite system can be easily controlled by chemical stoichiometry. Mitzi et al. reported that organic-based layered halide perovskites such as $(C_4H_9NH_3)_2(CH_3NH_3)_{n-1}Sn_nI_{3n+1}$ showed transition from semiconducting to metallic properties with increasing n (Mitzi et al., 1994). Further, Chung et al. demonstrated that an Sn-based perovskite exhibited high electrical conductivity and strong near-infrared photoluminescence (Chung et al., 2012).

Another key challenge with organo-inorganic hybrid perovskite materials is the instability of the organic cation in the A site. Organic cations such as $CH_3NH_3^+$ and $HC(NH_2)_2^+$ can suffer from compositional degradation at high temperatures and/or in humid atmospheres. To improve the stability of the perovskite, the organic cation in the A site is substituted with an alkali metal ion such as cesium (Cs) or rubidium (Rb) (Gou et al., 2017). However, inorganic perovskite materials based on a Cs ion in the A site exhibit temperature-sensitive phase transitions. Møller et al. demonstrated that the crystal structures of $CsPbCl_3$ and CsPbBr3 could be distorted even at room temperature (Møller, 1959).

Therefore, to overcome the disadvantage of inorganic perovskite materials based on Cs or Rb, it is necessary to consider alternatives to occupy the A site of perovskite materials. Thallium (Tl) is the heaviest nonradioactive element among p-block metals, which can exist as a monovalent or trivalent cation. Its chemical behavior closely resembles that of alkali metals (Salmon, 1963). Shand et al. reported that monovalent Tl compounds are more stable than trivalent thallium compounds (Shand et al., 1998). Tl could be the most promising candidate for perovskite materials because perovskite structures based on Tl show no phase transition induced by temperature (Stoeger, 1997). In addition, Tl-based perovskite structure such as $TlPbI_3$ has lower total energy than $CsPbI_3$ because a strong bond occurs between Tl and I (Liu et al., 2017). Khyzhun et al. demonstrated that $TlPbI_3$ single crystals could be grown in bulk form by using the Bridgman–Stockbarger technique (Khyzhun et al., 2016). However, this approach requires a high temperature and pressure to fabricate the single-crystal structure, presenting a limitation for diverse applications.

To solve the aforementioned limitations, we synthesized $TlSnX_3$ (X = Cl, Br, and I) perovskite structures as nanoparticles (NPs) by using ligands, dioleamide (DOA) and trioctylphosphine (TOP) ligands, which are strong reducing agents. By using the hot-injection method, $TlSnX_3$ NPs with high uniformity and crystallinity were obtained and applied to solution-processable optoelectronic devices. Furthermore, we demonstrate unique optoelectronic properties of Tl-based perovskite nanostructures, which have not been reported by downsizing perovskite nanostructures.

Materials and methods

Materials

Thallium (I) acetate (CH_3CO_2Tl, 99%), oleic acid ($CH_3(CH_2)_7CH{=}CH(CH_2)_7COOH$, 90%, OAc), oleylamine ($CH_3(CH_2)_7CH{=}CH(CH_2)_7CH_2NH_2$, 70%, OAm), tin (II) iodide (SnI_2, 99.99%), tin (II) bromide ($SnBr_2$, 99.99%), tin (II) chloride ($SnCl_2$, 99.99%), TOP (97%), anhydrous 1-butanol (99.8%), n-octane (extra pure, ≥99%), chlorobenzene (CB, anhydrous, 99.8%), acetonitrile (ACN, anhydrous, 99.8%), and Li-bis(trifluoromethanesulfonyl) imide (Li-TFSI) were purchased from Sigma Aldrich. Tin (IV) oxide (SnO_2 NPs, 15% in H_2O Colloidal dispersion) was purchased from Alfa Aesar. 2,20,7,70-Tetrakis(N,*N*-di-p-methoxyphenylamine)-9,90-spirobifluorene (Spiro-OMeTAD) and tris(2-(1Hpyrazol-1-yl)-4-tert-butylpyridine)-cobalt(III) tris(bis(trifluoromethylsulfonyl)imide) (FK209) were purchased from Lumtec. 2-Amylpyridine (≥98.0%) was purchased from TCI.

Synthesis of dioleamide (DOA)

DOA was prepared by adding a 1:1 molar mixture of OAc and OAm in a three-neck flask under an argon atmosphere. The mixture was then heated to 120 °C for 12 h with consistent, vigorous stirring. The reaction occurs through the dehydration condensation of the carboxylic group of OAc and the amine group of OAm (Cara et al., 2015). After the reaction was completed, the product was degassed under vacuum at 100 °C for 1 h to remove moisture generated during reaction. Finally, the resulting yellow liquid was cooled to room temperature and stored in the refrigerator.

Synthesis of $TlSnX_3$ NPs

DOA-capped $TlSnX_3$ nanoparticles (DOA-$TlSnX_3$ NPs) were synthesized using a modified hot-injection method (Protesescu et al., 2015). CH_3CO_2Tl (0.32 g), DOA (2 ml), and 1-octdecene (50 ml) were loaded into a three-neck flask and degassed under vacuum at 80 °C for 1 h. After the flask was filled with argon, the mixed solution was heated to 120 °C and vigorously stirred for 12 h until all the CH_3CO_2Tl was dissolved. Subsequently, the Tl precursor mixture was heated to 175 °C. After further stirring for 2 h, 5 ml of 1M solution of SnX_2 (X = Cl, Br, I) dissolved in TOP was injected into the prepared Tl precursor solution. Then, the mixed solution was heated at 170 °C for 10 s and then ice-cold water bath was placed under the three-neck flask to quench further $TlSnX_3$ NPs growth. Purification of the as-synthesized $TlSnX_3$ NPs were performed in an argon-filled glovebox. The resulting NPs in solution were washed by centrifugation (8,000 rpm, 5 min) three times with excess 1-butanol to remove surfactant residuals. The precipitated final products were dispersed in hexane. The supernatant was collected and stored in the dark at 4 °C for 48 h, after which the precipitated products were removed. The remaining n-hexane was dried under vacuum, and the dried $TlSnX_3$ NP pellets were redispersed in n-octane at a concentration of ~75 mg/mL.

Fabrication of $TlSnX_3$ NP-based solar cell device

Patterned indium tin oxide (ITO, 8 Ω/sq) substrates were sequentially cleaned by sonicating in detergent water, deionized water, acetone, and isopropyl alcohol for 10 min and then dried in an oven. Next, ultraviolet ozone (UVO) treatment was performed to remove the organic residues on the substrates. For the preparation of the electron transporting layer (ETL), SnO_2 NPs were diluted with deionized water at a weight ratio of 1:6. This solution was then deposited on UVO-treated ITO substrates by spin-coating at 3,000 rpm for 30 s, followed by annealing at 150 °C for 30 min. After transfer to the glovebox, to fabricate $TlSnX_3$ NP-based light-absorbing layers, a solution of $TlSnX_3$ NPs in n-octane (75 mg/mL) was spin-coated onto the SnO_2/ITO substrates at 1,000 rpm for 20 s, followed by 2000 rpm for 5 s. For the preparation of the hole-transporting layer, Spiro-OMeTAD was dissolved in CB with 39-μL 2-amylpyridine, 23-μL Li-TFSI (520 mg/mL in ACN), and 5-μL FK209 (180 mg/mL in ACN). This solution was spin-coated at 4,000 rpm for 30 s. Finally, an 80-nm-thick Au electrode was deposited by using a thermal evaporator.

Characterization of $TlSnX_3$ NPs and devices

Attenuated total reflectance-Fourier transform infrared spectroscopy (ATR-FTIR) (Nicolet iS50, Thermo Fisher Scientific) was used to characterize the synthesis of DOA. High-resolution transmission electron microscopy (HR-TEM) (FEI, TECNAI G^2 F30 ST, at 100 kV) was performed to investigate as-synthesized $TlSnX_3$ NPs. The crystal structure of the $TlSnX_3$ NPs was examined by an X-ray diffractometer (XRD) (Rigaku, DMAX-RB) operating at 20 kV and 200 mA with a rotating anode and Cu-K_α radiation of 0.15418 nm. X-ray photoelectron spectroscopy (XPS) was used to analyze the binding state of $TlSnX_3$ (X = Cl, Br, and I) by using an AXIS-HIS spectrometer with monochromatic Al K_α radiation (1,486.3 eV). XPS data were acquired in the range of 0–1,400 eV with a constant pass energy of 117.4 eV at a nominal photoelectron takeoff angle of 45°. The steady-state photoluminescence (PL) spectra of the $TlSnX_3$ NPs were obtained by excitation at 550 nm using a Fluorolog3-22 photoluminescence spectrometer system with a monochromator (iHR320, HORIBA Scientific). Commission Internationale de l'Eclairage (CIE) coordinates of $TlSnX_3$ NPs were measured using a visible-light spectrometer (DARSA PRO-5200, PSI) equipped with an integrating sphere at an applied current of 20 mA. The ultraviolet-visible (UV–Vis) absorption spectra of $TlSnX_3$ NPs were examined using a Lambda 35 spectrometer (PerkinElmer). Ultraviolet photoelectron spectroscopy (UPS) measurements were performed with a scanning XPS microprobe (PHI 5000 Versa Probe, Ulvac-PHI) using HeI (21.2 eV). The morphology of a $TlSnX_3$ NP film was analyzed by field-emission scanning electron microscopy (FE-SEM) (Verios G4 UC, FEI). Under an N_2 atmosphere, the current density–voltage (*J–V*) curves of the devices were measured using a Keithley 2,400 source under a xenon-lamp-based solar simulator (Newport 91160s, AAA class). A Si solar cell calibrated by the National Renewable Energy Laboratory was employed to adjust the light intensity to the AM 1.5G 1-sun condition (100 mW/cm^2). The voltage sweep rate was 20 mV with a delay of 20 ms for the reverse (forward) sweeping direction from 1.5 V (−0.1 V) to −0.1 V (1.5 V). The devices were evaluated using an SUS304 aperture with an area of 0.09 cm^2.

Results

Synthesis of $TlSnX_3$ NPs

Figure 1A illustrates the overall synthesis process of $TlSnX_3$ (X = Cl, Br, and I) perovskite NPs. Initially, Tl-oleate was prepared by vigorously agitating Tl^+ ions together with the synthesized DOA (step 1). For the preparation of Tl-oleate, we investigated various ligands to achieve the synthesis of highly dispersed $TlSnX_3$ nanoparticles in nonpolar solvents. However, $TlSnX_3$ NPs were not successfully synthesized when OAm or OAc was used as the ligand for the Tl ion. Moreover, the size and shape control of $TlSnX_3$ NPs by using these ligands is considerably challenging. To address these limitations, we synthesized DOA with two functional groups and employed it as an alternative ligand for the preparation of Tl precursors. DOA was synthesized by combining OAc and OAm in a 1:1 ratio. An angle of 120° between the carboxyl group of OAc and amine group of OAm leads to the formation of amide bonds between the acid and amine groups. As shown in Figure 1B, FTIR spectra indicate that the carboxyl acid peak of OAc and the amine peak of OAm have disappeared, which confirms the amide bonding. Thus, we demonstrate the presence of DOA with two functional groups. Subsequently, SnX_2 was dissolved in TOP, a coordinating ligand, under an inert atmosphere (step 2). TOP is a strong reducing agent that can prevent the oxidization to Sn^{4+} during the synthesis. Finally, this mixture was injected into a solution containing Tl-oleate at 170 °C, yielding colloidally stable $TlSnX_3$ NPs (for details, see the Experimental section). Figures 1C–E show $TlSnI_3$ NPs synthesized by using various ligands. When $TlSnI_3$ NPs were synthesized by using an OAm-Tl precursor, they exhibited aggregation (Figure 1C). Furthermore, the combination of OAc and OAm (the molar ratio of OAc/OAm = 80%) resulted in nonuniform and rectangular cube-shaped NPs (Figure 1D). By contrast, DOA-capped $TlSnI_3$ NPs showed high size uniformity without aggregation (Figure 1E). According to a previous study, as the ratio of OAc increases, the shape of Au NPs becomes anisotropic, and larger particles can be obtained because the excess OAc can adsorb on the specific facet (111) and hinder further growth of the (111) facet (Mohamed et al., 2010). Further, Calatayud et al. reported that the shape and size can be controlled by the ratio of OAc and OAm. An excess of OAc selectively binds to the {001} facets of TiO_2 NPs, which leads to a truncated octahedron or nanorod shape of TiO_2 NPs because of the higher electronegativity of the carboxylic group of OAc (Calatayud et al., 2013). Unlike the case of the combination of OAc and OAm (molar ratio of OAc/OAm = 80%), a high size uniformity of DOA-capped $TlSnI_3$ NPs is attributed to the pre-synthesized DOA ligand. Water molecules, which can degrade the perovskite structure, are the byproduct of the condensation between OAc and OAm (Cara et al., 2015). Thus, when the combination of OAc and OAm (the molar ratio of OAc/OAm = 80%) is used as the ligand, water molecules can be generated and degrade the perovskite structure during the synthesis process. On the contrary, as the water molecules are

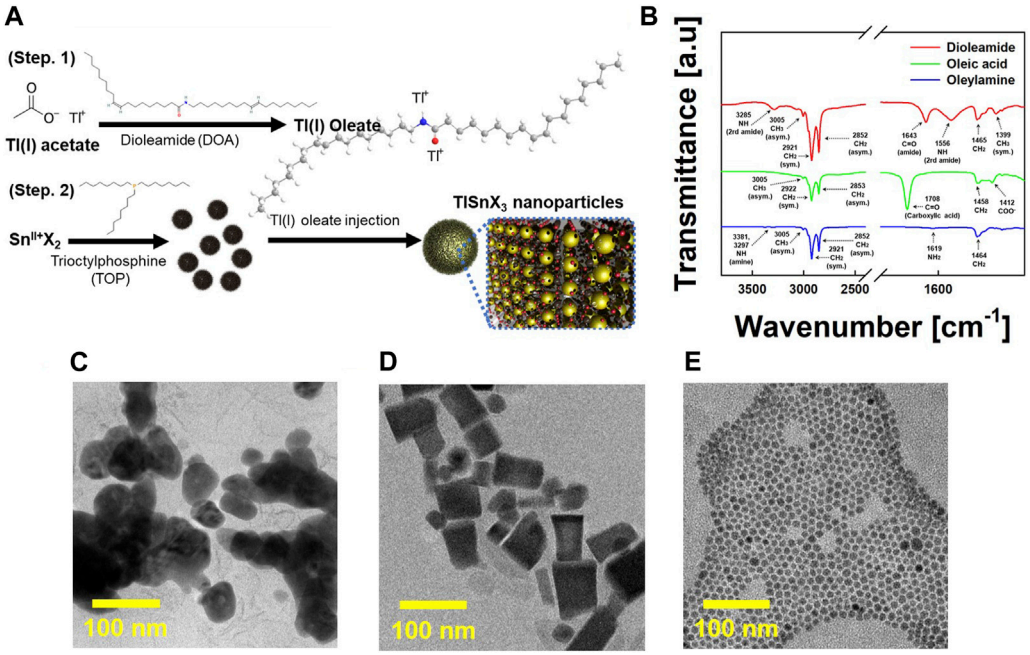

FIGURE 1
(A) Schematic of the synthesis process of $TlSnX_3$ nanoparticles (NPs) (X = Cl, Br, and I). **(B)** Fourier-transform infrared spectroscopy (FTIR) spectra of dioleamide (DOA, red), oleic acid (OAc, green), and oleylamine (OAm, blue). High-resolution (HR) transmission electron microscopy (HR-TEM) of $TlSnI_3$ perovskite NPs, synthesized by using **(C)** OAm, **(D)** the combination of OAc and OAm (the molar ratio of OAc/OAm = 80%) and **(E)** DOA.

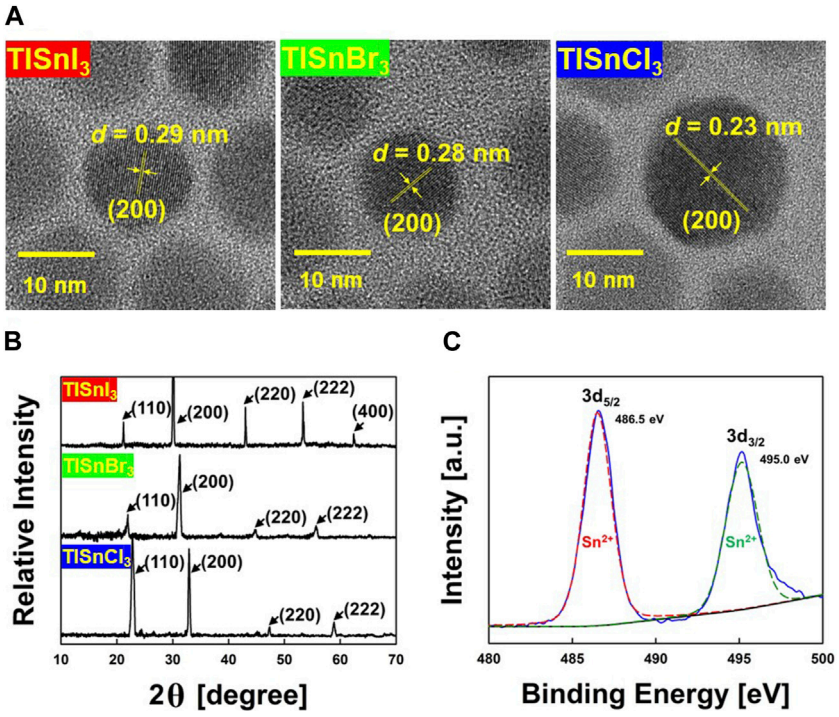

FIGURE 2
(A) HR-TEM Images of $TlSnI_3$ (left), $TlSnBr_3$ (middle), and $TlSnCl_3$ (right) perovskite NPs. **(B)** XRD patterns of $TlSnI_3$, $TlSnBr_3$, and $TlSnCl_3$ perovskite NPs. **(C)** X-ray photoelectron spectroscopy (XPS) spectra of as-synthesized $TlSnI_3$ perovskite NPs. The binding energy core levels of the Sn $3d_{3/2}$ and Sn $3d_{5/2}$ were measured at 494.5 and 486.9 eV, respectively.

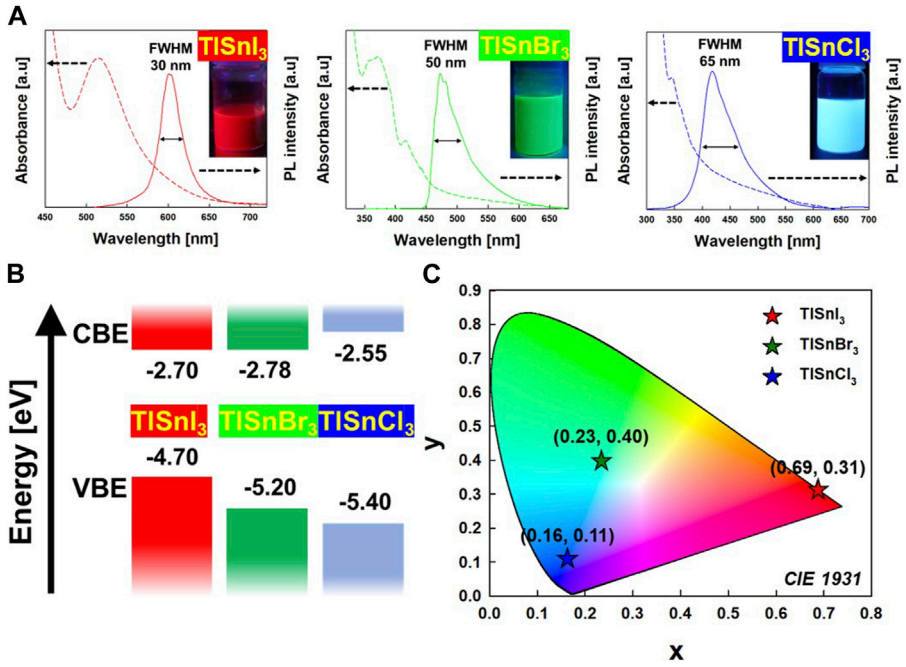

FIGURE 3
(A) Absorbance (dotted line) and photoluminescence (PL) (solid line) spectra of $TlSnI_3$ (left), $TlSnBr_3$ (middle), and $TlSnCl_3$ (right) perovskite NPs. **(B)** Band diagram of $TlSnI_3$ (red color), $TlSnBr_3$ (green color), and $TlSnCl_3$ (blue color) perovskite NPs. **(C)** The Commission Internationale del'Eclairage (CIE 1931) diagram of $TlSnI_3$ (red color), $TlSnBr_3$ (green color), and $TlSnCl_3$ (blue color) perovskite NPs.

pre-eliminated during the synthesis of the DOA ligand, the perovskite structure can be preserved, which results in the high size uniformity of $TlSnI_3$ NPs.

Structural and morphological characterization of $TlSnX_3$ NPs

The HR-TEM images in Figure 2A depict the DOA-capped $TlSnX_3$ NPs with various halogen ions at the X site (X = Cl, Br, and I) exhibiting high size uniformity (diameter: 15 nm) without aggregation. As shown in Figure 2B, all peaks in the XRD pattern indicate that DOA-capped $TlSnX_3$ perovskite NPs have a cubic crystal structure similar to that of $CsSnX_3$ NPs (Jellicoe et al., 2016). The broadening of the peaks observed in the XRD patterns, known as Scherrer broadening, can be attributed to the nano-sized formation of $TlSnX_3$ NPs. Interestingly, with halide ion substitution from I^- to $Br^-$to Cl^-, the 2θ values decreased. Notably, these trends have been frequently observed in cases of other metal halide perovskite analogues (Akkerman et al., 2015; Jang et al., 2015; Nedelcu et al., 2015). Supplementary Figure S1A depicts that Tl ions and halogen (X) ions occupy the (100) plane of the $TlSnX_3$ perovskite structure. The (100) plane is exposed to the outer surface of $TlSnX_3$, which affords a higher adsorption capacity of excess DOA ligands on the surface of $TlSnX_3$ NPs. These results demonstrate that $TlSnX_3$ NPs satisfy the Goldschmidt tolerance factor (Green et al., 2014). Thus, they can form stable cubic crystal structures (Supplementary Figure S1B).

The major challenge associated with Sn-based perovskite structures lies in their chemical instability when exposed to an ambient atmosphere because the presence of Sn^{2+} in the perovskite crystal structure makes them vulnerable to oxidation, which could lead to the formation of Sn^{4+}. Therefore, the TOP ligand was used as a reducing agent, which efficiently prevented the oxidation of Sn^{2+} within the perovskite structure. To assess the chemical stability of $TlSnX_3$ NPs, we performed XPS measurements. As observed in the XPS spectra in Figure 2C, there are two distinct peaks at 494.5 and 486.9 eV corresponding to the Sn $3d_{5/2}$ and Sn $3d_{3/2}$ transitions, respectively. For the passivation approach, two electrons are provided to the d-orbital of Sn by L-type ligands such as TOP and DOA, which effectively prevents the oxidation of Sn in the $TlSnX_3$ NCs (Shukla et al., 2003; Mourdikoudis and Liz-Marzán, 2013; Stranks et al., 2014). Thus, these results demonstrate that both TOP and DOA ligands contribute to the prevention of Sn oxidation, which thereby leads to the successful synthesis of a chemically stable cubic phase of $TlSnX_3$ NPs with high size uniformity.

Optical characterization of $TlSnX_3$ NPs

To investigate the optical properties of the $TlSnX_3$ NPs, absorbance and PL measurement were performed. In Figure 3A, the absorption onsets of $TlSnI_3$, $TlSnBr_3$, and $TlSnCl_3$ NPs are 601 nm (2.00 eV), 552 nm (2.42 eV), and 438 nm (2.85 eV), respectively. Further, the PL peaks of $TlSnX_3$ NPs are blue-shifted by substituting halide ions from I^- to Br^- to Cl^-. Specifically, $TlSnI_3$ NPs exhibited a red emission peak at 601 nm with a full width at half maximum (FWHM) of 30 nm, $TlSnBr_3$ NPs displayed a green emission peak at 472 nm with an FWHM of 50 nm, and $TlSnCl_3$ NCs showed a blue emission peak at 418 nm

10.3389/fmats.2023.1298188

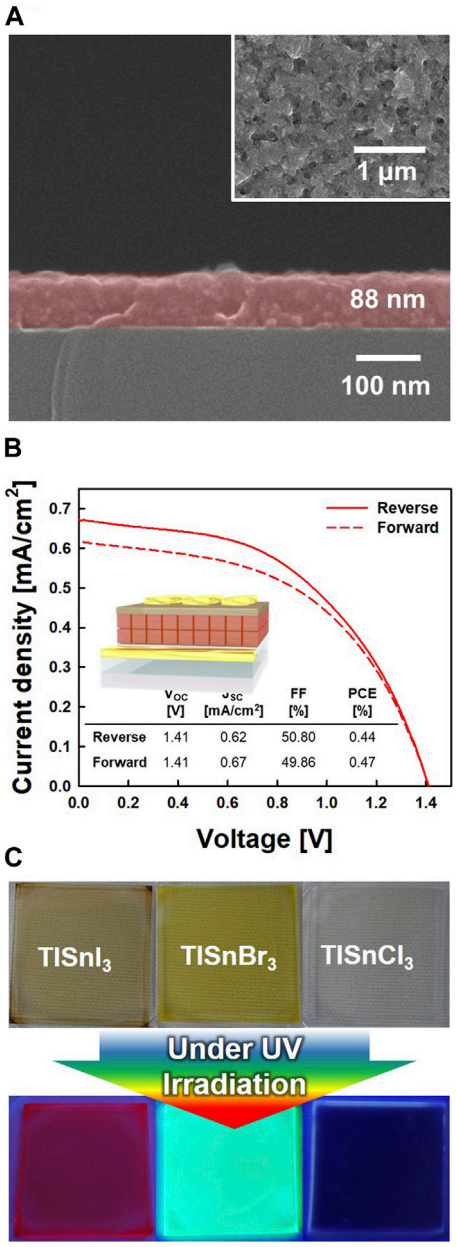

FIGURE 4
(A) Cross-section scanning electron microscopy (SEM) image of $TlSnI_3$ film coated on SnO_2 electron transporting layer (ETL) (Inset: surface SEM image of $TlSnI_3$ film). **(B)** Photocurrent density-voltage (*J-V*) curves of $TlSnI_3$ based perovskite solar cells (PSCs) measured at reverse (solid line) and forward (dotted line) scans. **(C)** The photographs of $TlSnI_3$ (red emission color), $TlSnBr_3$ (green emission color), and $TlSnCl_3$ (blue emission color) films under UV irradiation.

with an FWHM of 65 nm. Notably, $TlSnI_3$ NPs exhibited no Stokes shift, whereas $TlSnCl_3$ NPs exhibited a Stokes shift because of a stronger structural distortion in the excited state by a shorter Sn–Cl bond (Zhou et al., 2018). These results indicate that RGB color variation is achieved by modulating the halogen composition of $TlSnX_3$ NPs.

Moreover, we performed UPS measurements to investigate the precise position of the valence band and comprehend the electronic structure of the material. Figure 3B shows the energy band diagram of $TlSnX_3$. The electronic band structure is predominantly determined by the orbitals of $[SnX_6]^{4-}$ octahedra, with a minor contribution by electrons originating from the A site (Tl). The band gap of $TlSnX_3$ becomes larger by substituting halide ions (X) from I^- to Br^- and Cl^-. This trend is attributed to the increasing electronegativity of the halide ions (electronegativity: Cl > Br > I) (Matheu et al., 2022).

To investigate the emission colors of $TlSnX_3$ NPs, the CIE 1931 chromaticity diagram was used. This diagram displays the dominant emission color of a sample by using chromaticity coordinates (x, y), which represent the blue, green, and red constituents of the emission. These coordinates indicate the dominant emission colors displayed by the NPs. As shown in Figure 3C, the CIE coordinates of the red ($TlSnI_3$), green ($TlSnBr_3$), and blue ($TlSnCl_3$) emissions are (0.69, 0.31), (0.23, 0.40), and (0.16, 0.11), respectively. This CIE diagram is consistent with the PL spectra and photographs from solution emission color data (Figure 3A). These results confirm that $TlSnX_3$ NPs are attractive materials for optoelectronic applications.

Application of $TlSnX_3$ NPs to optoelectronic devices

As $TlSnI_3$ has a suitable electronic band structure for solar cells, we applied it as a light-absorption layer for PSCs. Cross-section SEM image shows that the $TlSnI_3$ was spin-coated on a SnO_2 ETL to fabricate an 88-nm-thick dense and crack-free film (Figure 4A). Figure 4B shows the photocurrent density–voltage (*J–V*) curves of the $TlSnI_3$-based PSCs (device structure of ITO/SnO_2/$TlSnI_3$/Spiro-OMeTAD/Au) under forward/reverse bias. The $TlSnI_3$-based PSC exhibited a short-circuit current density (J_{SC}) of 0.67 mA/cm^2, open-circuit voltage (V_{OC}) of 1.41 V, fill factor (*FF*) of 49.86%, and a PCE of 0.44% under forward bias. Despite the relatively low PCE of the $TlSnI_3$-based PSC, the high value of V_{OC} (1.41 V) demonstrates the feasibility of $TlSnI_3$ NPs for solar cell application. We can expect the improvement of photovoltaic performance by substituting the short-chain ligands for DOA ligands during the fabrication process of devices, which could mitigate the charge recombination and enhance the charge transport within the solar cell (Kim et al., 2019). Furthermore, we can use more precise coating method, such as the layer-by-layer method, to control the thickness of the $TlSnI_3$ layer, which could increase the light absorption capabilities and J_{SC} (Sanehira et al., 2017). Moreover, $TlSnX_3$ (X = I, Br, and Cl) films emitted vivid RGB colors, namely, red ($TlSnI_3$), green ($TlSnBr_3$), and blue ($TlSnCl_3$), which strongly support their feasibility for light-emitting devices (Figure 4C). These results demonstrate that $TlSnX_3$ (X = I, Br, and Cl) NPs are promising candidates for optoelectronic applications.

Discussion

In conclusion, we successfully synthesized $TlSnX_3$ (X = I, Br, Cl) NPs using DOA and TOP ligands, which are strong reducing agents. Both DOA and TOP ligands effectively prevent the oxidation of Sn^{2+}, which leads to a chemically stable cubic phase of $TlSnX_3$ NPs. Furthermore, we successfully tuned the optical bandgap of $TlSnX_3$

NPs by substituting different halides in the perovskite structure. The PL peaks of $TlSnX_3$ NPs were blue-shifted under halide ion substitution from I^- to Br^- to Cl^-. Additionally, according to the CIE 1931 diagram, the dominant emission colors by $TlSnI_3$, $TlSnBr_3$, and $TlSnCl_3$ were red, green, and blue, respectively. Moreover, the electronic structure determined by UPS and UV–Vis spectroscopy also demonstrated that with halide ion substitution from $I^-$to Br^- to Cl^-, the band gap of $TlSnX_3$ became larger, which facilitated the control of RGB color. On the basis of these results, $TlSnI_3$ NPs were used as light absorbers, and the fabricated device exhibited a J_{SC} of 0.67 mA/cm^2, V_{OC} of 1.41 V, *FF* of 49.86%, and PCE of 0.44% under forward bias. Furthermore, the $TlSnX_3$ (X = I, Br, and Cl) films emitted vivid RGB colors, which strongly support their feasibility for light-emitting devices. These results demonstrate that $TlSnX_3$ (X = I, Br, and Cl) NPs are promising candidates for optoelectronic applications. In the future, to enhance the performance of optoelectronic devices based on $TlSnX_3$ NPs, it is necessary to investigate the incorporation of additives or deposition processes, with the goal of preventing Sn^{2+} oxidation and controlling defects of $TlSnX_3$ NPs. Furthermore, it is vital to study the application of encapsulation layers or the insertion of interlayers to protect $TlSnX_3$ NPs from external stimuli. These studies will not only improve the long-term stability of $TlSnX_3$ NPs-based devices but also reduce the risk of metal ion leakage into the environment by the degradation of $TlSnX_3$ NPs (Babayigit et al., 2016; Vashishtha et al., 2018). Our research provides valuable insights into the utilization of $TlSnX_3$ NPs in optoelectronic devices, and further investigations hold the promise of enhancing its performance and stability.

Data availability statement

The original contributions presented in the study are included in the article/Supplementary Material, further inquiries can be directed to the corresponding authors.

Author contributions

WK: Data curation, Formal Analysis, Methodology, Writing–original draft. BK: Conceptualization, Formal Analysis, Methodology, Writing–original draft. MJK: Conceptualization, Methodology, Supervision, Writing–original draft, Writing–review and editing. HJ: Funding acquisition, Investigation, Methodology, Resources, Supervision, Writing–original draft, Writing–review and editing.

Funding

The authors declare financial support was received for the research, authorship, and/or publication of this article. This work was supported by the Korea Institute of Science and Technology (KIST) institutional programs (HJ). This work was supported by the Korea Institute of Energy Technology Evaluation and Planning (KETEP) grant funded by the Korea government (MOTIE) (20221B1010003B, Integrated High-Quality Technology Development of Remanufacturing Spent Cathode for Low Carbon Resource Recirculation) (MJK).

Conflict of interest

The authors declare that the research was conducted in the absence of any commercial or financial relationships that could be construed as a potential conflict of interest.

Publisher's note

Supplementary material

The Supplementary Material for this article can be found online at: https://www.frontiersin.org/articles/10.3389/fmats.2023.1298188/full#supplementary-material

References

Akkerman, Q. A., D'Innocenzo, V., Accornero, S., Scarpellini, A., Petrozza, A., Prato, M., et al. (2015). Tuning the optical properties of cesium lead halide perovskite nanocrystals by anion exchange reactions. *J. Am. Chem. Soc.* 137, 10276–10281. doi:10.1021/jacs.5b05602

Babayigit, A., Thanh, D. D., Ethirajan, A., Manca, J., Muller, M., Boyen, H.-G., et al. (2016). Assessing the toxicity of Pb- and Sn-based perovskite solar cells in model organism *Danio rerio*. *Sci. Rep.* 6, 18721. doi:10.1038/srep18721

Calatayud, D. G., Jardiel, T., Rodriguez, M., Peiteado, M., Fernandez-Hevia, D., and Caballero, A. C. (2013). Soft solution fluorine-free synthesis of anatase nanoparticles with tailored morphology. *Ceram. Int.* 39, 1195–1202. doi:10.1016/j.ceramint.2012.07.044

Cao, J., and Yan, F. (2021). Recent progress in tin-based perovskite solar cells. *Energy enivron. Sci.* 14, 1286–1325. doi:10.1039/D0EE04007J

Cara, C., Musinu, A., Mameli, V., Ardu, A., Niznansky, D., Bursik, J., et al. (2015). Dialkylamide as both capping agent and surfactant in a direct solvothermal synthesis of magnetite and titania nanoparticles. *Cryst. Growth Des.* 15, 2364–2372. doi:10.1021/acs.cgd.5b00160

Cho, H., Jeong, S.-H., Park, M.-H., Kim, Y.-H., Wolf, C., Lee, C.-L., et al. (2015). Overcoming the electroluminescence efficiency limitations of perovskite light-emitting diodes. *Science* 350, 1222–1225. doi:10.1126/science.aad1818

Chung, I., Song, J.-H., Im, J., Androulakis, J., Malliakas, C. D., Li, H., et al. (2012). $CsSnI_3$: semiconductor or metal? High electrical conductivity and strong near-infrared photoluminescence from a single material. High hole mobility and phase-transitions. *J. Am. Chem. Soc.* 134, 8579–8587. doi:10.1021/ja301539s

Gou, G., Young, J., Liu, X., and Rondinelli, J. M. (2017). Interplay of cation ordering and ferroelectricity in perovskite tin iodides: designing a polar halide perovskite for photovoltaic applications. *Inorg. Chem.* 56, 26–32. doi:10.1021/acs.inorgchem.6b01701

Green, M. A., Ho-Baillie, A., and Snaith, H. J. (2014). The emergence of perovskite solar cells. *Nat. Photonics* 8, 506–514. doi:10.1038/nphoton.2014.134

Jang, D. M., Park, K., Kim, D. H., Park, J., Shojaei, F., Kang, H. S., et al. (2015). Reversible halide exchange reaction of organometal trihalide perovskite colloidal nanocrystals for full-range band gap tuning. *Nano Lett.* 15, 5191–5199. doi:10.1021/acs.nanolett.5b01430

Jellicoe, T. C., Richter, J. M., Glass, H. F. J., Tabachnyk, M., Brady, R., Dutton, S. E., et al. (2016). Synthesis and optical properties of lead-free cesium tin halide perovskite nanocrystals. *J. Am. Chem. Soc.* 138, 2941–2944. doi:10.1021/jacs.5b13470

Khyzhun, O. Y., Fochuk, P. M., Kityk, I. V., Piasecki, M., Levkovets, S. I., Fedorchuk, A. O., et al. (2016). Single crystal growth and electronic structure of $TlPbI_3$. *Mat. Chem. Phys.* 172, 165–172. doi:10.1016/j.matchemphys.2016.01.058

Kim, J., Koo, B., Kim, W.-H., Choi, J., Choi, C., Lim, S. J., et al. (2019). Alkali acetate-assisted enhanced electronic coupling in $CsPbI_3$ perovskite quantum dot solids for improved photovoltaics. *Nano Energy* 66, 104130. doi:10.1016/j.nanoen.2019.104130

Kwon, N., Lee, J., Ko, M. J., Kim, Y. Y., and Seo, J. (2023). Recent progress of eco-friendly manufacturing process of efficient perovskite solar cells. *Nano Converg.* 10, 28. doi:10.1186/s40580-023-00375-5

Liu, Z., Zhang, T., Wang, Y., Wang, C., Zhang, P., Sarvari, H., et al. (2017). Electronic properties of a new all-inorganic perovskite $TlPbI_3$ simulated by the first principles. *Nanoscale Res. Lett.* 12, 232. doi:10.1186/s11671-017-2015-y

Luo, H., Li, P., Ma, J., Han, L., Zhang, Y., and Song, Y. (2022). Sustainable Pb management in perovskite solar cells toward eco-friendly development. *Adv. Energy Mat.* 12, 2201242. doi:10.1002/aenm.202201242

Matheu, R., Vigil, J. A., Crace, E. J., and Karunadasa, H. I. (2022). The halogen chemistry of halide perovskites. *Trends Chem.* 4, 206–219. doi:10.1016/j.trechm.2021.12.002

Mitzi, D. B., Feild, C. A., Harrison, W. T. A., and Guloy, A. M. (1994). Conducting tin halides with a layered organic-based perovskite structure. *Nature* 369, 467–469. doi:10.1038/369467a0

Mohamed, M. B., AbouZeid, K. M., Abdelsayed, V., Aljarash, A. A., and El-Shall, S. (2010). Growth mechanism of anisotropic gold nanocrystals via microwave synthesis: formation of dioleamide by gold nanocatalysis. *ACS Nano* 4, 2766–2772. doi:10.1021/nn9016179

Møller, C. K. (1959). The structure of caesium plumbo iodide $CsPbI_3$. *Mat. Fys. Medd. Dan. Vid. Selsk.* 32, 2.

Mourdikoudis, S., and Liz-Marzán, L. M. (2013). Oleylamine in nanoparticle synthesis. *Chem. Mat.* 25, 1465–1476. doi:10.1021/cm4000476

National Renewable Energy Laboratory (NREL) (2023). Best solar cell efficiencies chart. Available at https://www.nrel.gov/pv/assets/pdfs/best-research-cell-efficiencies.pdf (Accessed on July 26, 2023).

Nedelcu, G., Protesescu, L., Yakunin, S., Bodnarchuk, M. I., Grotevent, M. J., and Kovalenko, M. V. (2015). Fast anion-exchange in highly luminescent nanocrystals of cesium lead halide perovskites ($CsPbX_3$, X = Cl, Br, I). *Nano Lett.* 15, 5635–5640. doi:10.1021/acs.nanolett.5b02404

Pancini, L., Montecucco, R., Larini, V., Benassi, A., Mirani, D., Pica, G., et al. (2023). A fluorescent sensor to detect lead leakage from perovskite solar cells. *Mat. Adv.* 4, 2410–2417. doi:10.1039/D3MA00068K

Protesescu, L., Yakunin, S., Bodnarchuk, M. I., Krieg, F., Caputo, R., Hendon, C. H., et al. (2015). Nanocrystals of cesium lead halide perovskites ($CsPbX_3$, X = Cl, Br, and I): novel optoelectronic materials showing bright emission with wide color gamut. *Nano Lett.* 15, 3692–3696. doi:10.1021/nl5048779

Salmon, H. C. (1963). *The mining and smelting magazune*. Kessinger Publishing, LLC.

Sanehira, E. M., Marshall, A. R., Christians, J. A., Harvey, S. P., Ciesielski, P. N., Wheeler, L. M., et al. (2017). Enhanced mobility $CsPbI_3$ quantum dot arrays for record-efficiency, high-voltage photovoltaic cells. *Sci. Adv.* 3, eaao4204. doi:10.1126/sciadv.aao4204

Shand, P., Edmunds, W. M., and Ellis, J. (1998). *The hydrogeochemistry of thallium in natural waters" in Water–rock interaction: proceedings of the 9th International symposium on water–rock interaction*. 1st ed. Taupo, FL: CRC Press, 75–78.

Shukla, N., Liu, C., Jones, P. M., and Weller, D. (2003). FTIR study of surfactant bonding to FePt nanoparticles. *J. Magn. Magn. Mat.* 266, 178–184. doi:10.1016/s0304-8853(03)00469-4

Stoeger, W. (1997). The crystal structures of $TlPbI_3$ and Tl_4PbI_6. *Z. Naturforsch.* 32b, 975–981.

Stranks, S. D., Burlakov, V. M., Leijtens, T., Ball, J. M., Goriely, A., and Snaith, H. J. (2014). Recombination kinetics in organic-inorganic perovskites: excitons, free charge, and subgap states. *Phys. Rev. Appl.* 2, 034007. doi:10.1103/physrevapplied.2.034007

Takahashi, Y., Obara, R., Lin, Z.-Z., Takahashi, Y., Naito, T., Inabe, T., et al. (2011). Charge-transport tin-iodide perovskite $CH_3NH_3SnI_3$: origin of high conductivity. *Dalton Trans.* 40, 5563–5568. doi:10.1039/C0DT01601B

Vashishtha, P., Metin, D. Z., Cryer, M. E., Chen, K., Hodgkiss, J. M., Gaston, N., et al. (2018). Shape-size-and composition-controlled thallium lead halide perovskite nanowires and nanocrystals with tunable band gaps. *Chem. Mat.* 30, 2973–2982. doi:10.1021/acs.chemmater.8b00421

Xing, G., Mathews, N., Lim, S. S., Yantara, N., Liu, X., Sabba, D., et al. (2014). Low-temperature solution-processed wavelength-tunable perovskites for lasing. *Nat. Mat.* 13, 476–480. doi:10.1038/nmat3911

Xing, G., Mathews, N., Sun, S., Lim, S. S., Lam, Y. M., Grätzel, M., et al. (2013). Long-range balanced electron- and hole-transport lengths in organic-inorganic $CH_3NH_3PbI_3$. *Science* 342, 344–347. doi:10.1126/science.1243167

Zhang, Z., Kim, W., Ko, M. J., and Li, Y. (2023). Perovskite single-crystal thin films: preparation, surface engineering, and application. *Nano Converg.* 10, 23. doi:10.1186/s40580-023-00373-7

Zhou, C., Worku, M., Neu, J., Lin, H., Tian, Y., Lee, S., et al. (2018). Facile preparation of light emitting organic metal halide crystals with near-unity quantum efficiency. *Chem. Mat.* 30, 2374–2378. doi:10.1021/acs.chemmater.8b00129

Zhu, H., Fu, Y., Meng, F., Wu, X., Gong, Z., Ding, Q., et al. (2015). Lead halide perovskite nanowire lasers with low lasing thresholds and high quality factors. *Nat. Mat.* 14, 636–642. doi:10.1038/nmat4271